



Uncertainty quantification of conduction velocity in models of cardiac spread of activation

Anna Busatto^{1,2,3} · Lindsay C. R. Tanner^{1,2,3} · Jake A. Bergquist^{1,2,3} · Gernot Plank⁴ · Karli Gillette^{1,3} · Akil Narayan^{1,5} · Rob S. MacLeod^{1,2,3}

Received: 6 November 2025 / Accepted: 2 March 2026
© International Federation for Medical and Biological Engineering 2026

Abstract This study quantified the effect of conduction velocity (CV) variability on cardiac electrical activation patterns, a key factor for cardiac digital twins. We examined how myocardial and endocardial longitudinal, transverse, and sheet CVs influence ventricular activation across multiple pacing sites. Three porcine biventricular heart models, each including a fast-conducting endocardial layer, were used to simulate electrical activation with an eikonal approach. Uncertainty quantification with polynomial chaos expansion systematically varied six CV parameters within physiological ranges. In total, 1,868 simulations from eight ventricular pacing sites were analyzed for activation time, variability, and global sensitivities. Myocardial longitudinal CV showed the greatest influence on activation timing (global sensitivity up to 0.98). Endocardial-layer longitudinal CV was similarly important for endocardial stimuli, while transverse and sheet CVs had minimal effects. Activation-time variability reached 15 ms, increasing with distance from the pacing origin. Longitudinal CVs, particularly myocardial and endocardial-layer, dominate ventricular activation dynamics and should be prioritized when personalizing cardiac digital twins. Accounting for CV uncertainty is essential for accurate prediction and therapy optimization.

Keywords Biological simulations · Cardiac electrophysiology · Cardiac digital twin · Uncertainty quantification · Conduction velocity

1 Introduction

Computational models of cardiac function based on image-based anatomy and embedded cardiac electrophysiology (EP) have shown great promise in both research and potential clinical applications [1, 2]. When the computational models

are personalized to match individual patients based on clinical measurements, these models are termed patient-specific models of cardiac function or cardiac digital twins (CDTs) [3]. Such patient-specific models show great promise for personalized medicine, supporting diagnostics, prognostics, and treatment planning [4–6]. While efficiently personalizing anatomy from cardiac images has become feasible during the cardiac digital twinning process [7, 8], efficient estimation of patient-specific EP parameters from non-invasive measurements continues to be a major challenge [8–14]. These parameters include the membrane models assigned to each cell type, the passive electrical characteristics of both cell-to-cell coupling and extracellular conductivity, and the resulting macroscopic conduction velocity within the various myocardial tissues.

Two further elements of simulating cardiac electrical activity in the ventricles are the behavior of the conduction system and achieving efficient computational performance. Ventricular conduction is guided by the network of Purkinje fibers, the junctions with the working ventricular cells, and the resulting initiation of activation within the ventricles. Including all these elements explicitly in a model of the

✉ Anna Busatto
anna.busatto@utah.edu

¹ Scientific Computing and Imaging Institute, University of Utah, 72 S Central Campus Dr, Salt Lake City, UT 84112, USA

² Nora Eccles Cardiovascular Research and Training Institute, University of Utah, Salt Lake City, UT, USA

³ Department of Biomedical Engineering, University of Utah, Salt Lake City, UT, USA

⁴ Division of Biophysics and Medical Physics, Gottfried Schatz Research Center, Medical University of Graz, Graz, Austria

⁵ Department of Mathematics, University of Utah, Salt Lake City, UT, USA

ventricles quickly becomes computationally prohibitive, which has motivated various simplifications. Recent modeling studies of ventricular excitation have reproduced the initiation of the heartbeat by combining prescribed myocardial activation sites with a fast-conducting endocardial layer that approximates the functional role of the His–Purkinje system [8, 10, 15, 16]. To achieve the necessary overall computational efficiency, many contemporary studies have leveraged approximations driven by eikonal models of wave propagation to compute the spread of cardiac activation from these sites of early initiation [17–19].

Despite this progress, the volumetric conduction velocity (CV) tensor defining the spread of activation within the ventricular myocardium is commonly prescribed by homogeneous fixed anisotropy ratios for the myocardium, although exceptions exist [20–22]. The most typical anisotropy ratios used in modeling are either 3:1:1, 2:1:1, or 4:2:1 for longitudinal:transverse:sheet conduction, respectively, based on a wide range of reported experimental studies [23–29]. The fast-conducting endocardial layer is generally assigned simplified properties, ranging from isotropic conduction to scaled versions of these anisotropic myocardial values [15, 30–33]. Within this framework, the ventricular conduction velocity tensor can be described by six key parameters: myocardial longitudinal, transverse, and sheet CVs, together with endocardial-layer longitudinal, transverse, and sheet CVs. Accepting fixed values for these parameters reduces model complexity and reflects current limitations in obtaining accurate experimental or clinical measurements of CV with fine spatial resolution, particularly across a complex, curved volume like the heart [22, 34]. For a review on measuring CV in experimental and clinical settings, we refer to our previous work in Good et al. [22]. The major liability of keeping CV values constant and approximate is that the relationship between CV variability and the resulting activation sequences is largely unexplored.

Uncertainty quantification (UQ) is an approach that can address this gap by determining statistically the influence of variations in parameters on modeling outcomes [35–43]. A common UQ formulation is based on creating a polynomial chaos expansion (PCE) to approximate the underlying statistical relationships [44, 45]. PCE provides highly accurate output statistics with reduced numbers of evaluations of the driving model (compared to, e.g., Monte Carlo approaches) by leveraging mathematical assumptions about stochastic fields. Such characteristics are crucial when analyzing activation patterns stemming from variations in CVs, as the underlying models are computationally costly. To the best of our knowledge, UQ has never been applied to understand the specific effects of CV on the spread of activation in the heart.

We aimed to investigate how variations in CV affect activation patterns, using UQ within a PCE framework to analyze simulation models of cardiac EP. To achieve the computational performance needed for possible digital twin applications, we employed a fast and efficient eikonal solver to simulate cardiac activation from ventricular-paced beats [8, 18]. We strategically placed eight individual stimulation sites throughout the ventricular tissue based on theoretical and clinical pacing locations, allowing us to assess the epicardial, mid-myocardial, and endocardial regions of the heart separately. Additionally, we computed activation metrics to characterize the activation patterns.

Our results highlight the importance of tuning myocardial and endocardial longitudinal CV parameters within physiological ranges to accurately capture heterogeneities in cardiac activation patterns, particularly for beats stimulated from the endocardium. This consideration is crucial for reliable and personalized cardiac electrophysiology modeling.

2 Methods

We explored the role of conduction velocity (CV) variations on total activation times within three biventricular geometric models derived from post-experiment imaging of porcine hearts. Into these models, we incorporated a fast-conducting endocardial layer as a simplification of the Purkinje system [16, 46]. We applied the polynomial chaos expansion (PCE) as a means to quantify uncertainty in the simulations of propagation using a computationally efficient approximation (the eikonal approach) and evaluated the impact of variations in six parameters: myocardial longitudinal CV, myocardial transverse CV, myocardial sheet CV, endocardial-layer longitudinal CV, endocardial-layer transverse CV, and endocardial-layer sheet CV.

2.1 Model generation

Three bi-ventricular geometric models of porcine hearts were generated from computerized tomography (CT) scans, as shown in Fig. 1 Panel A. The tissue acquisition was approved by the University of Utah IACUC (Protocol #20-11001) following all institutional animal care guidelines. These models were derived through segmentation using Seg3D [47] and transformed into finite-element meshes with a mean edge length of approximately 800 μm to ensure adequate resolution for eikonal-based simulations [18, 47–49]. Universal ventricular coordinates (UVCs) were computed for each ventricular mesh to allow for consistency across different geometries [8, 50]. Myocardial fiber orientations were incorporated into each

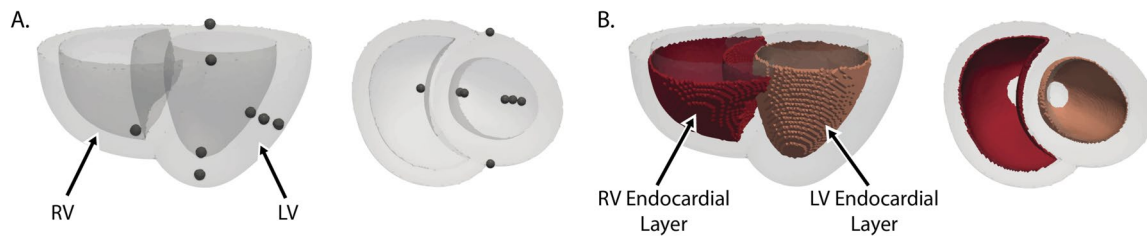


Fig. 1 Biventricular cardiac geometry including stimulation points and endocardial layer. Front view (panel A left) and top view (panel A right) of the geometry and stimulation point locations. Front view (panel B left) and top view (panel B right) of the geometry and endocardial layer

geometry using a standard rule-based approach [50]. Fiber directions were prescribed using a smoothly varying primary fiber angle, rotating from approximately -60° at the epicardium to $+60^\circ$ at the endocardium, together with a helix fiber angle component ranging from approximately 0° at the epicardium to -35° at the endocardium, consistent with established ventricular fiber architecture reported in anatomical studies [51]. The resulting fiber field was applied uniformly across all geometries and held fixed for all simulations to isolate the effects of conduction velocity variability. A fast-conducting endocardial layer was incorporated as a single-element layer into each mesh and acted as a surrogate for the His–Purkinje system. We refer to the conduction velocities assigned to this surrogate region as *endocardial-layer* conduction velocities to distinguish them from myocardial tissue properties. The layer extended from 15% to 90% of the apicobasal distance (captured by the apicobasal UVC coordinate z), based on imaging studies [52] of the His–Purkinje system.

2.2 Conduction velocity parameter ranges

For both the endocardial layer and the working myocardium, we assigned three CV ranges corresponding to the longitudinal, transverse, and sheet directions. The longitudinal CV of the working myocardium ranged between 50 cm/s and 80 cm/s [53]. In comparison, the longitudinal CV in the endocardial layer was four to five times higher than that in the surrounding myocardium. The CVs of the transverse and sheet directions for the endocardial layer were set to range from 0.5–1.0 times the longitudinal CVs [23–29]. The result was a set of six parameters in Table 1, which we varied independently and systematically following a uniform distribution over physiological ranges based on the literature, focusing on obtaining realistic values of overall activation time [20, 54, 55]. PCE does not require independent or uniformly distributed inputs. Rather, it requires specifying a joint probability model for the uncertain parameters, which determines the orthogonal polynomial basis used in the expansion. In this study, we assumed (i) independent parameters and (ii) uniform

Table 1 Conduction velocity parameter ranges

Parameter	Minimum value	Maximum value
Myocardial longitudinal (M_L)	50 cm/s	80 cm/s
Myocardial transverse (M_T)	$1/3 M_L$	$2/3 M_L$
Myocardial sheet (M_S)	$1/3 M_L$	$2/3 M_L$
Endocardial-layer longitudinal (E_L)	200 cm/s	400 cm/s
Endocardial-layer transverse (E_T)	$1/2 E_L$	$1 E_L$
Endocardial-layer sheet (E_S)	$1/2 E_L$	$1 E_L$

marginal distributions over physiologically plausible bounds (Table 1). This choice reflects limited and inconsistent evidence for the joint distribution of myocardial and endocardial-layer conduction parameters across subjects, particularly in the context of a simplified fast-conducting endocardial layer rather than an explicit conduction system. As such, uniform independent sampling provides a conservative, bounded uncertainty model appropriate for sensitivity ranking under broad plausible variability.

2.3 Uncertainty quantification framework

To quantify the uncertainty in CV, we employed polynomial chaos expansion (PCE) through our open-source tool UncertainSCI [45, 56]. This approach involves approximating the dependence of a specific product of the simulation on a finite set of random parameters using a multivariate polynomial function derived from a modest set of simulations with specific parameter values. This approximation then serves as an emulator to solve the underlying propagation simulation [36, 57, 58].

2.3.1 Setting hyperparameters for uncertainty quantification

A key practical requirement to conduct a UQ analysis with UncertainSCI is to set hyperparameters that control the sample points and ultimately the quality of the resulting polynomial expansion [59]. A first step is to control the order of the polynomial, which, in turn, guides—but does not dictate—the number of sample points required to build

the PCE model. For this study, we tested orders 5 to 10 and selected polynomial order 6, based on a strategy developed in previous studies [59, 60].

We constructed the PCE surrogate non-intrusively using a regression (least-squares) fit to a set of eikonal simulations evaluated at selected parameter points [45, 56]. For a total-degree expansion of order p in d parameters, the number of polynomial basis terms is

$$N_{\text{basis}} = \binom{d+p}{p}, \quad (1)$$

so that with $d = 6$ and $p = 6$, $N_{\text{basis}} = \binom{12}{6} = 924$ coefficients must be determined. In practice, stable regression requires a number of model evaluations that is at least comparable to N_{basis} , and modest oversampling is commonly used to improve numerical conditioning and reduce sensitivity to the particular sampled design. For our chosen (d, p) setting, UncertainSCI provided a default design with 934 samples ($N_{\text{basis}} = 924$, plus oversampling with 10 additional samples), slightly exceeding N_{basis} . This choice of default in UncertainSCI is based on prior experience using PCE, and UncertainSCI performs internal quality checks on the samples after the default number have been generated. We then doubled the design to 1868 simulations to further improve robustness of the estimated moments and Sobol indices across pacing sites, consistent with prior observations [60].

A second step requires setting the distribution and ranges applied to the input parameters, in our case, the values for CV. The samples were selected from uniformly distributed values within the boundaries of Table 1. We used the doubled sample size (1868 simulations) for all subsequent analyses to ensure consistency and robustness across pacing protocols, following observations from prior studies [59, 60].

2.4 Eikonal-based simulation of cardiac electrophysiology

The underlying simulation model for our study employed a well-known wave-based approach based on an eikonal approximation implemented within the framework of the *Cardiac Arrhythmia Research Package* (CARP) [8, 18, 61]. The resulting simulations included 1868 runs that generated activation maps within the ventricles. The eikonal formulation can be summarized as follows:

$$\begin{cases} \sqrt{\nabla t_a^T \mathbf{V} \nabla t_a} = 1 & \text{in } \Omega \\ t_a = t_o & \text{in } \Gamma, \end{cases} \quad (2)$$

In this formulation, Ω denotes the myocardial domain, and t_a represents the scalar function describing the arrival time of the depolarization wavefront at position x . The boundary Γ specifies the region where activation is initiated, corresponding in our case to single-pacing sites with prescribed activation time t_o . The CV tensor \mathbf{V} varies with each set of sample values of CV in the longitudinal, transverse, and sheet fiber directions, according to the formula:

$$\mathbf{V} := v_l^2 \mathbf{l}\mathbf{l}^T + v_t^2 \mathbf{t}\mathbf{t}^T + v_s^2 \mathbf{s}\mathbf{s}^T, \quad (3)$$

where v_l , v_t , and v_s are the velocities associated with \mathbf{l} , \mathbf{t} , and \mathbf{s} , which are the longitudinal, transverse, and sheet fiber directions, respectively.

2.5 Stimulus points

We initiated the simulations of activation from eight distinct sites: epicardial, mid-myocardial, and endocardial sites originating from the same location in the left ventricular (LV) free wall; apical LV epicardial and endocardial sites; a single apical right ventricular (RV) endocardial site; and sites at the epicardial posterior and anterior ventricular junctions. Figure 1 Panel A shows the location of these sites on the geometry. These stimulation sites made up the locations in Γ and activated at $t_o = 0$. To maintain consistency across all three geometries, these stimulation sites were identified using UVCs from the geometric model, as explained above and summarized in Table 2.

2.6 Computing quantities of interest

The analysis encompassed various metrics, including total volumetric activation time, as well as identification of the location and timing of the earliest and latest activation sites on the epicardial surface. Epicardial breakthrough was defined as the earliest phase of epicardial activation. For each simulation, we first identified the total epicardial activation time T_{epi} , defined as the difference between the earliest and latest epicardial activation times. The

Table 2 UVC stimulus locations

Location	z	ρ	ϕ	ν
LV Epi.	0.5	1	π	-1
LV Mid.	0.5	0.5	π	-1
LV Endo.	0.5	0	π	-1
LV Apex Epi.	0	1	π	-1
LV Apex Endo.	0	0	π	-1
RV Apex Endo.	0.1	0	0	1
Anterior junction	1	1	$\frac{\pi}{2}$	-1
Posterior junction	1	1	$-\frac{\pi}{2}$	-1

breakthrough region was then defined as the portion of the epicardial surface that becomes activated within the first 10% of this total epicardial activation interval. Formally, this region consists of epicardial locations with activation times satisfying

$$t_a \leq t_{\min}^{\text{epi}} + 0.1 T_{\text{epi}},$$

where t_{\min}^{epi} denotes the earliest epicardial activation time. The area of the breakthrough was computed as the total surface area of epicardial mesh elements meeting this criterion. This relative-time definition provides a robust, geometry-independent measure of early epicardial activation that adapts naturally to variations in overall activation duration.

From the PCE model, we computed the mean, standard deviation (STD), and parameter sensitivities through straightforward and computationally efficient polynomial manipulations. The sensitivity analysis was performed using Sobol indices, also known as sensitivity indices ($S_{\mathcal{I}}$), which quantify the extent to which a model’s output variance is affected by a subset of its input variables. The specific formulas used for the statistical analysis are:

$$\begin{aligned} &\text{Mean} && \mathbb{E}[t_a], \\ &\text{STD} && \sqrt{\mathbb{E}[(t_a - \mathbb{E}[t_a])^2]}, \\ &\text{Global Sensitivity} && \text{Given } \mathcal{I} \subset \{1, \dots, d\}, S_{\mathcal{I}} = \frac{\text{STD}(t_a; \mathcal{I})^2 - \sum_{\emptyset \neq \mathcal{J} \subsetneq \mathcal{I}} \text{STD}(t_a; \mathcal{J})^2}{\text{STD}(t_a)^2}. \end{aligned} \tag{4}$$

where \mathbb{E} is the expected value, t_a is the activation time (computed as a scalar-valued UQ emulator), and p are the d parameters (in our setting $d = 6$, as in Table 1). For the global sensitivity, the summation is taken over all nonempty strict subsets $\mathcal{J} \subsetneq \mathcal{I}$, where \mathcal{J} and \mathcal{I} are subsets of the parameter indices $\{1, 2, \dots, d\}$. In particular, $\text{STD}(t_a; \mathcal{I})$ denotes the (partial) standard deviation attributed to the parameter subset \mathcal{I} , as obtained from the variance decomposition of the PCE surrogate.

Sobol sensitivity indices were computed pointwise over the ventricular volume, yielding spatial maps of parameter influence. Because pointwise sensitivities can exhibit localized peaks (e.g., near stimulation sites, within the endocardial-layer region, or in late-activating territories), we interpret multiple complementary measures when assessing parameter importance. In particular, spatially aggregated sensitivities (such as the spatial mean and spatial patterns across the ventricular volume) are used to assess global influence, while maximum sensitivities are reported to highlight localized regions where variability in a given parameter exerts a strong effect. Accordingly, conclusions regarding dominant parameters are supported primarily by consistent spatial patterns and spatially aggregated measures across pacing sites, rather than by isolated peak values alone.

3 Results

3.1 Epicardial, mid-myocardial, and endocardial left ventricular free wall stimulation

Figure 2 shows the mean, STD, and global sensitivities for epicardial, mid-myocardial, and endocardial LV free wall stimulus sites on the ventricular volume, given changes in the six conduction velocity (CV) parameters described above. The total activation time reported for the mean values showed a decrease from 96 ms following epicardial stimulation to 82 ms after mid-myocardial stimulation and 71 ms after endocardial stimulation. The mean pattern of excitation for epicardial stimulation showed concentric, approximately elliptical isochrones on the ventricular surface in the vicinity of the pacing site, as observed in previous research studies [34]. Although less distinct, similar patterns, but with a rotated central axis, were observed after mid-myocardial and endocardial stimulations. The ranges of values of STD for each pacing site were roughly similar, but both minima and maxima generally decreased from epicardial to mid-myocardial to endocardial stimulations. In particular, the STD ranged between 4.4 ms and 15 ms for epicardial stimulation, between 3.9 ms and 12 ms for mid-myocardial stimulation, and between 3.1 ms and 10 ms for endocardial stimulation. As expected, the STDs were lowest close to the stimulus sites and increased as activation spread through the rest of the heart.

For the global sensitivities, there was a complex interaction between the dominant parameters and the pacing location. For example, following LV epicardial stimulation, the myocardial longitudinal CV exhibited the largest spatially aggregated influence on activation dynamics, with a mean sensitivity of 0.43 and localized peak sensitivities reaching 0.95. This was followed by the myocardial transverse CV, which showed a lower but still substantial spatially aggregated influence (mean sensitivity of 0.34), with localized peak sensitivities up to 0.56. The other CVs played only minimal roles in the variability of the spread of activation initiated on the epicardium. The same general findings, with reduced amplitudes, appeared following LV mid-myocardial stimulation. The myocardial longitudinal CV again exhibited the largest spatially aggregated influence on activation dynamics, with a mean global sensitivity of 0.30 and localized peak sensitivities reaching 0.71. The myocardial transverse and endocardial-layer longitudinal CVs showed comparable but lower spatially aggregated influence, with mean global sensitivities of 0.20 and 0.23, respectively, and localized peak sensitivities of 0.49 and 0.56. Following LV endocardial stimulation, there were similar ranges of impacts of the three major

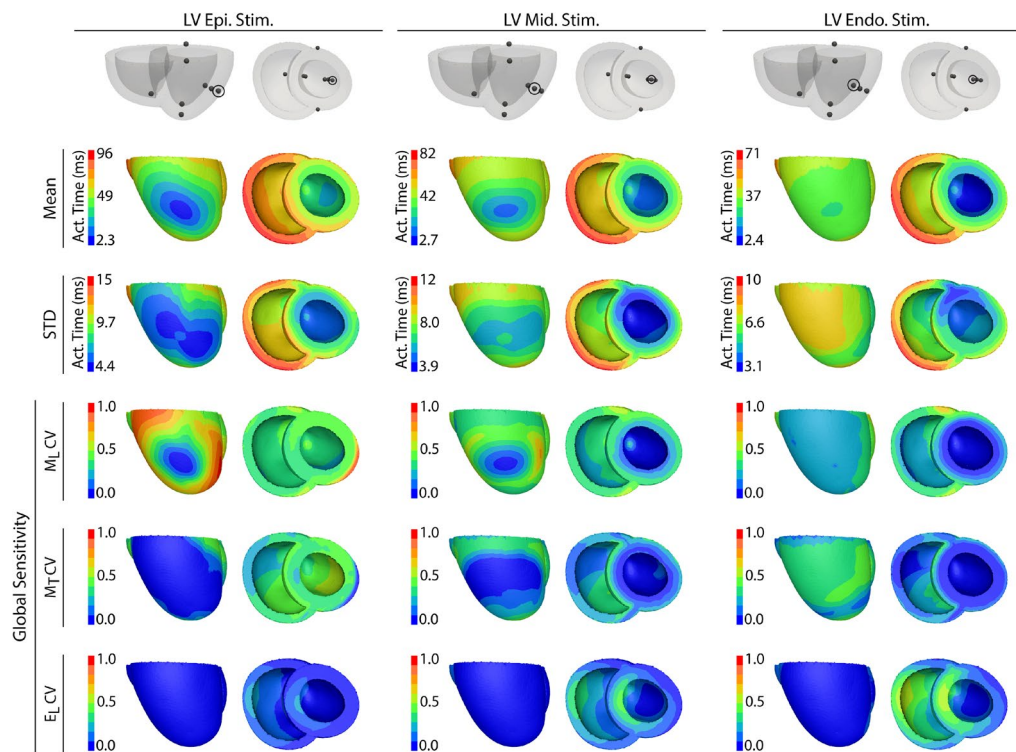


Fig. 2 Uncertainty quantification of volumetric activation times following left ventricular epicardial (left), mid-myocardial (center), and endocardial (right) stimulations. The first row shows the location of the geometry (front and top view). The second row shows the mean activation sequence; the third row shows the standard deviation; the fourth, fifth, and sixth rows show the global sensitivity contributions of variations in the myocardial longitudinal (row three),

myocardial transverse (row four), and endocardial-layer longitudinal (row five) conduction velocities, respectively. In each column, there are views from two perspectives, the left lateral and the basal-to-apical views of the heart, respectively. For the global sensitivities, M_L CV refers to the myocardial longitudinal conduction velocity, M_T CV to the myocardial transverse conduction velocity, and E_L CV to the endocardial-layer longitudinal conduction velocity

CV values, but some different spatial patterns. The myocardial longitudinal and endocardial-layer longitudinal CVs exhibited comparable spatially aggregated influence on activation dynamics, each with a mean sensitivity of 0.23, indicating similar global importance under this pacing condition. Localized peak sensitivities reached 0.67 for the myocardial longitudinal CV and 0.64 for the endocardial-layer longitudinal CV, reflecting region-specific effects. In contrast, the myocardial transverse CV showed a lower spatially aggregated influence (mean sensitivity of 0.20), with localized peak sensitivities up to 0.51. The spatial patterns of the sensitivities showed even greater variations, e.g., with only a small basoposterior region of high sensitivity to myocardial longitudinal CV. The strong dependence on the endocardial-layer CV was also uniquely visible in the endocardial sides of the RV free wall and the septum. Across the sampled CV space, total volumetric activation time varied widely for LV free-wall stimulation. In particular, the LV endocardial site showed the broadest spread among all protocols (min 46 ms, max 149 ms; range 103 ms), consistent with the strong sensitivities reported above. The location of the earliest epicardial

activation (breakthrough) had a STD of 2.5 mm, and 2.4 mm following mid-myocardial and endocardial stimulation, respectively. For the area of the breakthrough site on the epicardial surface, the means were 202 mm² and 853 mm², while the STDs were 44.4 mm² and 382 mm², respectively. The location of the latest site of activation had a larger STD with 3.7 mm, 3.5 mm, and 3.0 mm following epicardial, mid-myocardial, and endocardial stimulation, respectively.

3.2 Left ventricular epicardial and endocardial apex, right ventricular endocardial apex stimulation

Figure 3 shows the mean activation times, their STDs, and global sensitivities for stimulus sites at the LV epicardial and endocardial apex, and RV endocardial apex in response to variations in the six CV parameters described above. The longest total ventricular activation time was observed following LV epicardial apex stimulation (mean 91 ms), compared to 72 ms for LV endocardial apex stimulation and 78 ms for RV endocardial apex stimulation. In all cases, concentric isochrones emerged from the

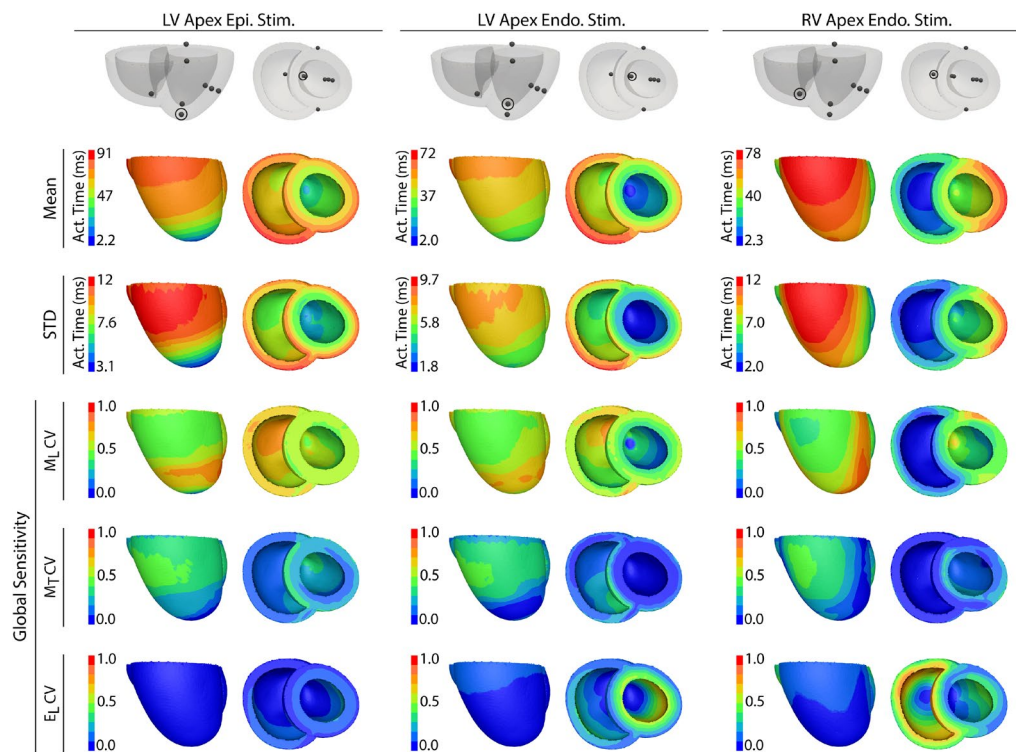


Fig. 3 Uncertainty quantification of volumetric activation times following LV epicardial apex (left), LV endocardial apex (center), and RV endocardial apex (right) stimulations. The first row shows the location of the stimuli on the geometry (front and top views). The second row shows the mean activation sequence; the third row shows the standard deviation; the fourth, fifth, and sixth rows show the global sensitivity contributions of variations in the myocardial longitudinal (row three),

myocardial transverse (row four), and endocardial-layer longitudinal (row five) conduction velocities, respectively. In each column, there are views from two perspectives, the left lateral and the basal-to-apical views of the heart, respectively. For the global sensitivities, M_L CV refers to the myocardial longitudinal conduction velocity, M_T CV to the myocardial transverse conduction velocity, and E_L CV to the endocardial-layer longitudinal conduction velocity

stimulation site and spread in patterns that reflected the local fiber orientation. For LV epicardial and endocardial apex stimulation, the isochrones moved vertically from apex to base, while for RV endocardial apex stimulation, they spread quickly from the endocardial RV apex to eventually cross the septum and then spread toward the LV base of the heart. The STD values had similar ranges for each pacing site, i.e., roughly 2–12 ms, and the distributions were consistent in that values were smallest near the stimulus sites and were greatest in the areas of late activation.

For the global sensitivities, following LV epicardial apex stimulation, the myocardial longitudinal CV exhibited the largest spatially aggregated influence on activation dynamics, with a mean sensitivity of 0.57 and localized peak sensitivities reaching 0.91, followed by the myocardial transverse CV, which showed a lower but still substantial spatially aggregated influence (mean sensitivity of 0.26), with localized peak sensitivities up to 0.44. The spread of activation was much less affected by the myocardial sheet CV and the endocardial-layer CVs (longitudinal, transverse, and sheet). Among these, the endocardial-layer

longitudinal CV showed only a minor spatially aggregated influence (mean sensitivity 0.06), with localized peak sensitivities up to 0.27 that were confined to a small endocardial region. Following LV endocardial apex stimulation, the myocardial longitudinal CV again exhibited the strongest spatially aggregated influence on activation dynamics (mean sensitivity of 0.50), with localized peak sensitivities reaching 0.88 and the highest values arising in the apical RV region. The endocardial-layer longitudinal CV followed with a smaller spatially aggregated influence (mean sensitivity of 0.17), despite localized peak sensitivities reaching 0.74 that were largely confined to the LV subendocardium. The myocardial transverse and sheet CVs played smaller roles, with mean sensitivities of 0.18 and 0.04 and localized peak sensitivities of 0.47 and 0.35, respectively. When the RV endocardial apex was stimulated, the endocardial-layer longitudinal CV exhibited the largest localized sensitivities (peak value 0.89), primarily within the RV endocardial free wall, while the myocardial longitudinal CV showed the largest spatially aggregated influence (mean sensitivity 0.34), and also exhibited broad regions of elevated sensitivity (localized peaks up to 0.86)

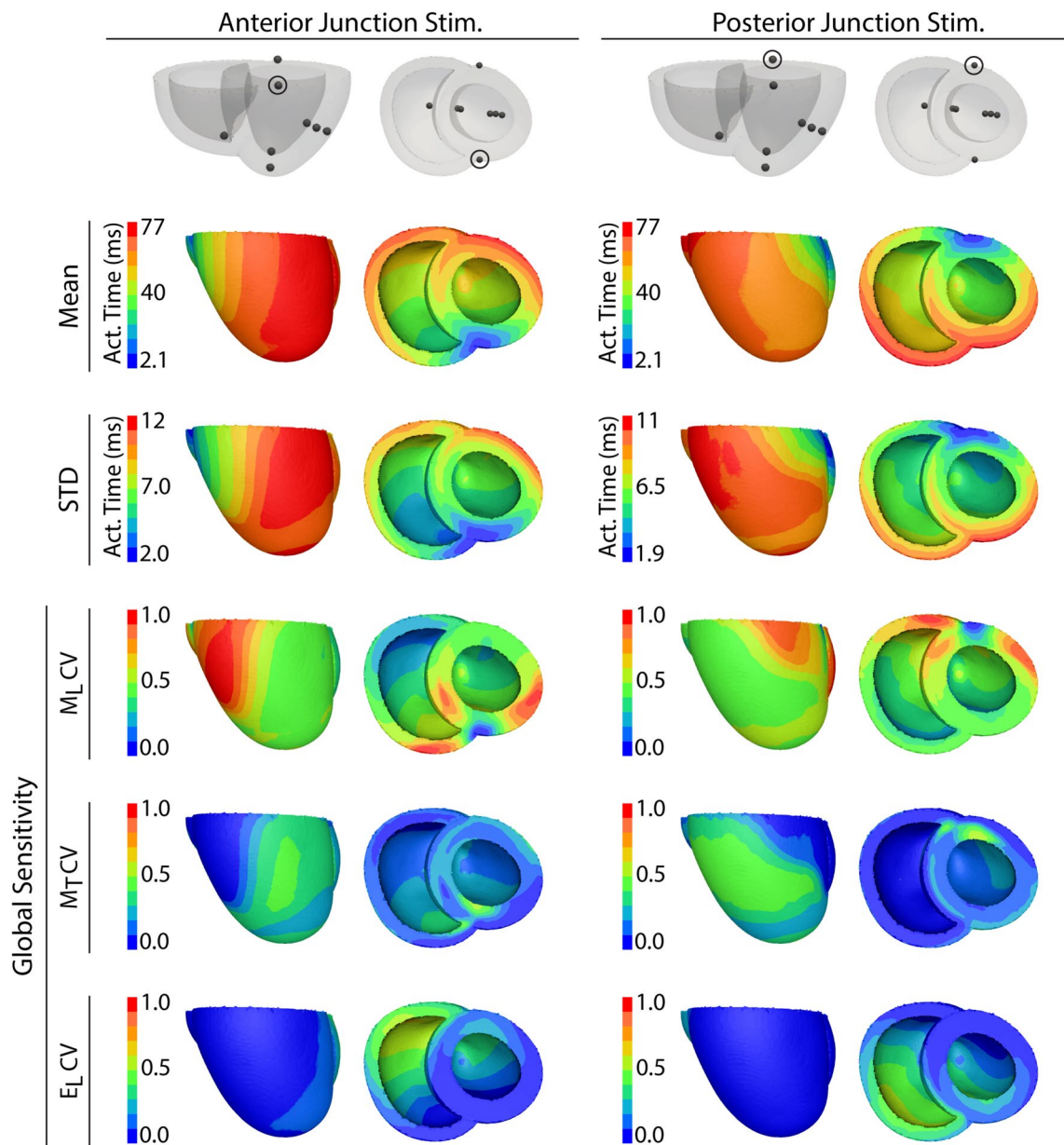


Fig. 4 Uncertainty quantification of volumetric activation times following anterior junction (left) and posterior junction (right) stimulations. The first row shows the location of the stimuli on the geometry (front and top views). The second row shows the mean activation sequence; the third row shows the standard deviation; the fourth, fifth, and sixth rows show the global sensitivity contributions of variations in the myocardial longitudinal (row three), myocardial transverse (row

four), and endocardial-layer longitudinal (row five) conduction velocities, respectively. In each column, there are views from two perspectives, the left lateral and the basal-to-apical views of the heart, respectively. For the global sensitivities, M_L CV refers to the myocardial longitudinal conduction velocity, M_T CV to the myocardial transverse conduction velocity, and E_L CV to the endocardial-layer longitudinal conduction velocity

across the LV and RV epicardium. In contrast, the myocardial transverse and sheet CVs had relatively smaller spatially aggregated effects, with mean sensitivities of 0.16 and 0.03 and localized peak sensitivities of 0.49 and 0.41, respectively. The location of the earliest site of activation on the epicardium had small values of STD of 1.6 mm and 1.9 mm following RV endocardial apex stimulation and LV endocardial apex stimulation, respectively. For the

area of the breakthrough site on the epicardial surface, the means for RV and LV endocardial apex stimulation were 386 mm² and 496 mm², with large STDs of 198 mm² and 175 mm², respectively. The location of the latest site of activation had larger STD values, with 1.5 mm, 3.4 mm, and 3.6 mm following LV epicardial apex stimulation, RV endocardial apex stimulation, and LV endocardial apex stimulation, respectively.

3.3 Anterior and posterior junction stimulations

Figure 4 shows the mean, STD, and global sensitivities for anterior and posterior junction stimulations of the ventricular activation, given changes in the six CV parameters. The means showed the same maximum activation of 77 ms following both anterior and posterior junction stimulations. Visually, the activation sequences from the two stimulations followed mirror patterns, with each activation time spreading from the stimulation point toward the other side of the heart, either anterior to posterior or vice versa. The STDs had similar values and followed a similarly symmetric pattern, ranging between 2.0 ms and 12 ms after anterior junction stimulation and between 1.9 ms and 11 ms following posterior junction stimulation. Similarly to the activation times, the STDs were lowest in areas close to the stimulation sites and gradually increased towards the termination sites.

The global sensitivities again revealed the dominance of the myocardial longitudinal CV in influencing the spread of activation. Following anterior junction stimulation, the myocardial longitudinal CV exhibited the largest spatially aggregated influence on activation dynamics, with a mean sensitivity of 0.45 and localized peak sensitivities reaching 0.97, followed by the endocardial-layer longitudinal CV, which showed a smaller spatially aggregated influence (mean sensitivity of 0.18) despite localized peak sensitivities reaching 0.62. The patterns were also highly anti-symmetric, with areas of high sensitivity to variability in longitudinal CV aligning with areas of low sensitivity to transverse CV. The myocardial transverse and sheet CVs still played a modest but relevant role in the spread of activation, with mean sensitivities of 0.24 and 0.04 and localized peak sensitivities of 0.55 and 0.47, respectively. Following posterior junction stimulation, the myocardial longitudinal CV again exhibited the strongest spatially aggregated influence on overall activation behavior, with a mean sensitivity of 0.49 and localized peak sensitivities reaching 0.98. The endocardial-layer longitudinal CV showed a lower spatially aggregated influence (mean sensitivity of 0.17), despite localized peak sensitivities reaching 0.60, closely followed by the myocardial transverse and sheet CVs, which exhibited smaller spatially aggregated effects, with mean sensitivities of 0.19 and 0.08 and localized peak sensitivities of 0.57 and 0.49, respectively. The asymmetry of the spread of activation was not perfect, however, as the location of the latest site of activation had a STD of 8.0 mm for anterior activation and 5.5 mm for posterior. The anterior and posterior junction stimulation protocols exhibited narrower, but still substantial, variation across CV samples. For the anterior junction, total activation time ranged from 52.22 ms to 125.36 ms (range 73.14 ms), representing the smallest spread among the sites we tested.

4 Discussion

In this study, we aimed to explore the impact of conduction velocity (CV) variations on myocardial activation patterns, with a particular focus on the longitudinal, transverse, and sheet components of both myocardial and endocardial-layer CV. Our results offer valuable insights into how variations in CV components influence the spread of activation across different stimulation sites, with implications for both simulation accuracy and clinical applications. The results also highlight which CV parameters should be prioritized when running cardiac electrophysiology simulations to improve both predictive modeling and real-world clinical predictions. Throughout the Discussion, statements regarding parameter importance are based primarily on spatially aggregated sensitivity measures and consistent spatial patterns observed across pacing sites, while localized peak sensitivities are interpreted as indicators of region-specific effects rather than global dominance.

4.1 The importance of myocardial longitudinal conduction velocity

Across all tested stimulation sites, the myocardial longitudinal CV consistently exerted the strongest influence on the spread of activation, as reflected by the highest spatially aggregated (mean) sensitivity values across the ventricular volume. This trend was observed for both epicardial and endocardial stimulations, with global sensitivities reaching up to 0.98 at the posterior junction and 0.95 at the LV epicardium. These results are not surprising and highlight the crucial role of myocardial longitudinal conduction in the overall behavior of activation. One possible explanation is that myocardial longitudinal conduction dominates because it governs propagation through the majority of the ventricular volume. Although endocardial-layer longitudinal CV is faster in absolute terms, it is confined to a thin layer, whereas myocardial longitudinal CV influences activation across the bulk of the myocardium. This result is consistent with previous experimental studies [34], which also showed that the longitudinal axis plays a key role in dictating activation patterns across the ventricles.

Given its strong influence, myocardial longitudinal CV should be a primary focus in both simulations and experimental investigations of ventricular activation, and accurate modeling of this parameter is crucial for predicting the effects of therapies that seek to adjust the timing of cardiac activation, such as cardiac resynchronization therapy (CRT). Future studies should investigate how variations in longitudinal CV impact the efficacy of CRT and other conduction-targeting therapies.

A related consistent result is the extent of the variation observed (by means of STDs) when CV values were varied, reaching as high as 15 ms in some cases, and hence of critical importance when reconstructing activation sequences under normal or abnormal conditions. A general finding from the spatial patterns of STD is that activation shows more variability the further away from the site of earliest activation, e.g., on the right ventricular epicardium following LV pacing.

While the longitudinal CV value was typically the most powerful influence on the activation sequences, this dominance was by no means complete. The myocardial transverse CV also played a relevant role, as evidenced by the differences between the patterns of STD and those of the global sensitivities. In some cases, these patterns were similar for different pacing conditions, but in others, the transverse CV contributed significantly to the variability in activation times. This suggests that both longitudinal and transverse CVs should be carefully considered when predicting activation dynamics.

Personalization strategies for cardiac digital twins often focus on reproducing whole-heart activation timing measures, such as QRS duration or total ventricular activation time [15]. Our results indicate that CV parameters, particularly myocardial and endocardial-layer longitudinal CVs, should also be explicitly considered in this process. The sensitivity we observed is comparable to the typical adjustments needed to match overall timing metrics, with STDs around 10–15 ms and site-specific variations ranging from ~70–100+ ms. These magnitudes imply that uncertainty in CVs can materially shift predicted activation times, reinforcing the need to (i) prioritize calibration of myocardial longitudinal CV, (ii) account for endocardial-layer longitudinal CV when beats originate near the endocardium, and (iii) report uncertainty bands on model-derived timing measures used during personalization. Importantly, the prioritization of CV parameters discussed here is conditional on the paced-beat excitation patterns, the healthy ventricular substrates examined in this study, and the nature of the calibration targets. Under alternative excitation scenarios, such as conduction-system pacing, multi-site or CRT protocols, or abnormal rhythms involving conduction block or reentry, the relative importance of transverse and sheet conduction components may increase. Similarly, when calibration targets emphasize surface ECG features (e.g., QRS duration) rather than activation-time metrics, parameters such as transverse or sheet CV may become more identifiable and should be prioritized accordingly. In such cases, sensitivity rankings should be re-evaluated using excitation patterns and data targets appropriate to the clinical context. Our findings are also consistent with recent studies reporting that variations in myocardial fiber helix angle have

limited influence on global electrical activation timing [62, 63]. Taken together with the present results, this body of work supports the interpretation that macroscopic activation timing is more strongly governed by effective longitudinal conduction properties than by physiologically plausible variations in fiber helix angle observed in healthy human populations [51]. Accordingly, uncertainty in longitudinal conduction parameters is expected to exert a larger influence on activation timing than uncertainty in fiber helix angle in the scenarios examined here.

4.2 Endocardial-layer longitudinal conduction velocity: site-specific influence

Not surprisingly, the role of endocardial-layer longitudinal CV was more pronounced following endocardial stimulation sites. For example, after LV endocardial apex stimulation, the global sensitivity to the endocardial-layer longitudinal CV reached values of 0.74, approaching the sensitivity to the myocardial longitudinal CV (0.88). Similarly, findings emerged following RV endocardial apex stimulation, in which the endocardial-layer longitudinal CV had a maximum sensitivity of 0.89, slightly exceeding that of the myocardial longitudinal CV at 0.86. Such findings suggest that endocardial-layer CVs should be carefully considered when stimulation occurs near or at the endocardium, as is the case in both sinus beats and typical pacemaker implants. Importantly, the influence of endocardial-layer longitudinal CV was largely localized to subendocardial regions and pacing-dependent, consistent with its lower spatially aggregated sensitivity compared to myocardial longitudinal CV. We also note that imposing a layer of rapid conduction near the endocardium is only a surrogate for the role of the Purkinje network, and our results support the importance of this network in overall activation [16].

4.3 Minimal impact of myocardial sheet and endocardial-layer transverse CVs

In this study, we observed that variations in the myocardial sheet and endocardial-layer transverse CVs had a relatively minimal impact on the spread of activation and the overall activation times. This result is reflected in the low global sensitivity values for these parameters, especially compared to myocardial longitudinal CV. For example, across all stimulation sites, the myocardial sheet and endocardial-layer transverse CVs exhibited low spatially aggregated sensitivities, with localized peaks that remained below 0.5. These findings suggest that, even for most scenarios in which activation is driven from epicardial or endocardial sites, the myocardial sheet and endocardial-layer transverse CVs play a limited role in altering activation patterns. Consequently,

the values assigned to these parameters are unlikely to substantially affect the simulation outcomes for these common pacing scenarios. However, these results do not rule out the potential relevance of myocardial sheet and endocardial-layer transverse CVs in specific situations, such as those involving more complex or pathological substrates. Further studies exploring these parameters in conditions like myocardial fibrosis, ischemia, or in models with highly heterogeneous tissue properties may reveal circumstances where these CV components exert more influence.

4.4 Variation in activation time and spatial spread

A consistent finding from all our studies was that the total volumetric activation time decreased as the stimulation site moved from the epicardium to the endocardium, with activation times at the LV epicardial site averaging 96 ms, compared to 82 ms following mid-myocardial pacing, and 71 ms after LV endocardial pacing. This progression aligns with the known physiological property that endocardial sites often exhibit faster activation than epicardial ones. Physiologically, this difference is attributed to the orientation of myocardial fibers and the role of the rapid conduction in the subendocardial region due to the Purkinje network [64]. In simulations, the longitudinally oriented fibers in the endocardium approximate this behavior and facilitate faster conduction compared to the more transverse orientation of the epicardial fibers.

Similarly to total activation times, their variance also decreased as stimulation moved deeper into the myocardium, reflecting more consistent activation with endocardial versus epicardial stimulation. These results underscore the importance of considering both the location of stimulation and the corresponding CV variations when predicting activation dynamics. Moreover, they hint at the relative instability of PVCs that initiate from the epicardial surface and their possibly enhanced potential to generate sustained arrhythmias [65–68]. The variability in the location of activation was greater at epicardial sites, with larger STDs observed in regions of late activation compared to those that activated earlier. This result suggests that activation near the epicardium may be more prone to spatial variability, likely due to the more complex geometry and heterogeneity of conduction in that region.

4.5 Limitations

Our study has some limitations that should be considered when interpreting these results. First, we exclusively applied single-paced protocols rather than conduction system pacing (CSP) protocols. CSP has emerged as a more physiological alternative to right ventricular pacing and is increasingly

being used in select cases for cardiac resynchronization therapy [69]. We plan to incorporate CSP protocols in future work to explore their potential and compare their impact with the findings presented here. However, many arrhythmias are initiated by ectopic activations, and so there is considerable interest in understanding the subsequent activation patterns. Additionally, we modeled activation under relatively normal, smoothly varying fiber structures, which may have only partially captured the complex heterogeneity of CV across the heart. The variation in CV within different regions, especially in the face of substrate changes due to ischemia or fibrosis, will certainly impact the spread of activation, and this complexity warrants further exploration. While our study focused primarily on healthy conditions, understanding normal physiological behavior is crucial before delving into more complex scenarios, such as pathological conditions where myocardial ischemia or infarction may alter electrophysiological substrates.

Another important limitation is that we did not include an explicit, branching His–Purkinje system (HPS). Instead, we employed a simplified fast-conducting endocardial layer as a surrogate, which captures some functional effects of rapid subendocardial propagation but cannot reproduce pathway-specific delays, discrete Purkinje–myocyte junction properties, or bundle-level abnormalities. Furthermore, our simulations were based on an eikonal approximation, which is computationally efficient but simplifies the full bidomain formulation. As such, it neglects wavefront curvature effects, source–sink interactions, and transmembrane dynamics that can become critical in pathological settings or in the presence of conduction block. These modeling choices were deliberate for tractability in large-scale uncertainty quantification, but they constrain physiological fidelity and should be kept in mind when interpreting our findings. Therefore, future studies will need to investigate the impact of altered CV in diseased hearts to better understand its implications in clinical settings. Finally, because this study focuses on single-site pacing in otherwise healthy ventricles, the reported sensitivity rankings should not be interpreted as universally applicable across all excitation patterns. In pathological conditions or complex pacing configurations, anisotropic propagation mechanisms associated with transverse and sheet conduction may become more influential. Extending the present analysis to such scenarios is an important direction for future studies.

5 Conclusion

We quantified how uncertainty in CV components propagates to activation timing in ventricular eikonal simulations across multiple pacing sites. Three consistent findings

emerged. First, myocardial longitudinal CV dominated the variability of activation, with global sensitivities up to 0.98 and spatially broad influence across all pacing configurations. Second, endocardial-layer longitudinal CV became comparably influential whenever activation originated near the endocardium (e.g., LV free wall endocardial and LV/RV apical endocardial sites), underscoring the need to parameterize subendocardial conduction with care. Third, myocardial sheet and endocardial-layer transverse CVs contributed little to global activation metrics in otherwise healthy hearts paced from single sites.

Across stimulation sites, total volumetric activation time decreased from epicardial to mid-myocardial to endocardial pacing, while the standard deviation increased with distance from the stimulus, reaching ~ 15 ms in late-activating regions. These effects imply that personalizing myocardial longitudinal CV should be a primary target for cardiac digital twins and therapy planning, and reporting uncertainty bands on activation maps is important for interpreting model-based predictions.

Practically, our results suggest a prioritization strategy for parameter personalization: calibrate myocardial longitudinal CV first, then endocardial-layer longitudinal CV for endocardially initiated beats, and finally refine transverse/sheet components where indicated by data. Future work should extend this analysis to conduction-system pacing, multi-site/CRT protocols, and pathological substrates (e.g., fibrosis, ischemia), and evaluate tighter data assimilation pipelines that estimate CVs directly from noninvasive measurements.

Acknowledgements Computational support for this research came from the Center for Integrative Biomedical Computing (www.sci.utah.edu/cibc).

Author Contributions A.B., K.G., G.P., A.N., and R.S.M. contributed to the conception and design of the study. A.B., L.C.R.T., J.A.B., K.G., A.N., and R.S.M. were involved in the acquisition, analysis, or interpretation of data. All authors participated in drafting the manuscript or revising it critically for important intellectual content, approved the final version, and agree to be accountable for all aspects of the work to ensure the accuracy and integrity of any part of the research is appropriately investigated and resolved. All individuals who meet authorship criteria are listed.

Funding The research leading to these results received funding from the National Institutes of Health under grant agreements P41 GM103545, R24 GM136986, T32 HL007576, and U24EB029012, the NSF GRFP, the Nora Eccles Harrison Foundation for Cardiovascular Research, and grant ESP 592 from the Austrian Science Fund.

Data Availability The simulated data that support the findings of this study are not publicly available, but are available from the corresponding author upon reasonable request.

Declarations

Ethical Approval The tissue acquisition was approved by the University of Utah IACUC (Protocol #20-11001) following all institutional animal care guidelines.

Consent to Participate Not applicable.

Consent to Publish Not applicable.

Conflicts of Interests The authors have no competing interests to declare that are relevant to the content of this article.

References

- Niederer SA, Lumens J, Trayanova NA (2019) Computational models in cardiology. *Nat Rev Cardiol* 16:100–111
- Cluitmans M, Walton R, Plank G (2023) Editorial: Computational methods in cardiac electrophysiology. *Front Physiol* 14:1231342
- Jiang X, Vadhavkar S, Ye Y, Toloubidokhti M, Missel R, Wang L (2024) HyPer-EP: Meta-Learning Hybrid Personalized Models for Cardiac Electrophysiology
- Arevalo HJ, Vadakkumpadan F, Guallar E, Jebb A, Malamas P, Wu KC, Trayanova NA (2016) Arrhythmia risk stratification of patients after myocardial infarction using personalized heart models. *Nat Commun* 7:11437. Publisher: Nature Publishing Group
- Boyle PM, Zghaib T, Zahid S, Ali RL, Deng D, Franceschi WH, Hakim JB, Murphy MJ, Prakosa A, Zimmerman SL et al (2019) Computationally guided personalized targeted ablation of persistent atrial fibrillation. *Nature biomedical engineering* 3(11):870–879
- ...Corral-Acero J, Margara F, Marciniak M, Rodero C, Loncaric F, Feng Y, Gilbert A, Fernandes JF, Bukhari HA, Wajdan A, Martinez MV, Santos MS, Shamohammadi M, Luo H, Westphal P, Leeson P, DiAchille P, Gurev V, Mayr M, Geris L, Pathmanathan P, Morrison T, Cornelussen R, Prinzen F, Delhaas T, Doltra A, Sitges M, Vigmond EJ, Zacur E, Grau V, Rodriguez B, Remme EW, Niederer S, Mortier P, McLeod K, Potse M, Pueyo E, Bueno-Orovio A, Lamata P (2020) The “Digital Twin” to enable the vision of precision cardiology. *Eur Heart J* 41:4556–4564
- Prassl AJ, Kicking F, Ahammer H, Grau V, Schneider JE, Hofer E, Vigmond EJ, Trayanova NA, Plank G et al (2009) Automatically generated, anatomically accurate meshes for cardiac electrophysiology problems. *IEEE Trans Biomed Eng* 56(5):1318–1330
- Gillette K, Gsell MA, Prassl AJ, Karabelas E, Reiter U, Reiter G, Grandits T, Payer C, Štern D, Urschler M, Bayer JD, Augustin CM, Neic A, Pock T, Vigmond EJ, Plank G (2021) A framework for the generation of digital twins of cardiac electrophysiology from clinical 12-lead ECGs. *Med Image Anal* 71:102080
- Cárdenes R, Sebastian R, Soto-Iglesias D, Berrueto A, Camara O (2015) Estimation of Purkinje trees from electro-anatomical mapping of the left ventricle using minimal cost geodesics. *J-MIA* 24(1):52–62
- Barber F, Langfield P, Lozano M, Garcia-Fernandez I, Duchateau J, Hocini M, Haissaguerre M, Vigmond E, Sebastian R (2021) Estimation of Personalized Minimal Purkinje systems from human electro-anatomical maps. *IEEE Trans Med Imaging* 40:2182–2194
- Camps J, Lawson B, Drovandi C, Mincholé A, Wang ZJ, Grau V, Burrage K, Rodriguez B (2021) Inference of ventricular

- activation properties from non-invasive electrocardiography. *Med Image Anal* 73:102143
12. Pezzuto S, Prinzen FW, Potse M, Maffessanti F, Regoli F, Caputo ML, Conte G, Krause R, Auricchio A (2021) Reconstruction of three-dimensional biventricular activation based on the 12-lead electrocardiogram via patient-specific modelling. *EP Europace* 23:640–647
 13. Grandits T, Verhulsdonk J, Haase G, Effland A, Pezzuto S (2023) Digital twinning of cardiac electrophysiology models from the surface ECG: A geodesic backpropagation approach. *IEEE Trans Biomed Eng* pp 1–8. Conference Name: IEEE Transactions on Biomedical Engineering
 14. Li L, Camps J, Rodriguez B, Grau V (2024) Solving the Inverse Problem of Electrocardiography for Cardiac Digital Twins: A Survey. *arXiv preprint arXiv:2406.11445*
 15. Cardone-Noott L, Bueno-Orovio A, Mincholé A, Zenzemi N, Rodriguez B (2016) Human ventricular activation sequence and the simulation of the electrocardiographic QRS complex and its variability in healthy and intraventricular block conditions. *EP Europace* vol 18, no suppl_4, pp iv4-iv15
 16. Camps J, Berg LA, Wang ZJ, Sebastian R, Riebel LL, Doste R, Zhou X, Sachetto R, Coleman J, Lawson B et al (2024) Digital twinning of the human ventricular activation sequence to clinical 12-lead ECGs and magnetic resonance imaging using realistic Purkinje networks for in silico clinical trials. *Med Image Anal* 94:103108
 17. Franzone PC, Guerri L (1993) Spreading of excitation in 3-D models of the anisotropic cardiac tissue. I. validation of the eikonal model. *Math Biosci* 113:145–209
 18. Neic A, Campos FO, Prassl AJ, Niederer SA, Bishop MJ, Vigmond EJ, Plank G (2017) Efficient computation of electrograms and ECGs in human whole heart simulations using a reaction-eikonal model. *J Comput Phys* 346:191–211
 19. Pezzuto S, Kal'avský P, Potse M, Prinzen FW, Auricchio A, Krause R (2017) Evaluation of a Rapid Anisotropic Model for ECG Simulation. *Front Physiol* 8:265
 20. Good WW, Erem B, Zenger B, Coll-Font J, Brooks DH, MacLeod RS (2018) Temporal Performance of Laplacian Eigenmaps and 3D Conduction Velocity in Detecting Ischemic Stress. *J Electrocardiol* 51:S116–S120
 21. Jæger KH, Edwards AG, McCulloch A, Tveito A (2019) Properties of cardiac conduction in a cell-based computational model. *PLoS Comput Biol* 15:e1007042
 22. Good WW, Gillette KK, Zenger B, Bergquist JA, Rupp LC, Tate J, Anderson D, Gsell MA, Plank G, MacLeod RS (2021) Estimation and Validation of Cardiac Conduction Velocity and Wavefront Reconstruction Using Epicardial and Volumetric Data. *IEEE Trans Biomed Eng* 68:3290–3300
 23. Clerc L (1976) Directional differences of impulse spread in trabecular muscle from mammalian heart. *J Physiol* 255(2):335–346
 24. Roberts DE, Hersh LT, Scher AM (1979) Influence of cardiac fiber orientation on wavefront voltage, conduction velocity, and tissue resistivity in the dog. *Circ Res* 44(5):701–712
 25. Spach MS, Miller W 3rd, Geselowitz DB, Barr RC, Kootsey JM, Johnson EA (1981) The discontinuous nature of propagation in normal canine cardiac muscle. Evidence for recurrent discontinuities of intracellular resistance that affect the membrane currents. *Circ Res* 48(1):39–54
 26. Roberts DE, Scher AM (1982) Effect of tissue anisotropy on extracellular potential fields in canine myocardium in situ. *Circ Res* 50(3):342–351. Publisher: Am Heart Assoc
 27. Hooks DA, Trew ML, Caldwell BJ, Sands GB, LeGrice IJ, Smaill BH (2007) Laminar arrangement of ventricular myocytes influences electrical behavior of the heart. *Circ Res* 101(10):e103–e112
 28. Caldwell BJ, Trew ML, Sands GB, Hooks DA, LeGrice IJ, Smaill BH (2009) Three distinct directions of intramural activation reveal nonuniform side-to-side electrical coupling of ventricular myocytes. *Circulation: Arrhythmia and Electrophysiology* 2(4):433–440
 29. Johnston BM (2016) Six Conductivity Values to Use in the Bidomain Model of Cardiac Tissue. *IEEE Trans Biomed Eng* 63:1525–1531
 30. Draper MH, Weidmann S (1951) Cardiac resting and action potentials recorded with an intracellular electrode. *J Physiol* 115:74–94
 31. Kassebaum D, Van Dyke A (1966) Electrophysiological effects of isoproterenol on Purkinje fibers of the heart. *Circ Res* 19(5):940–946
 32. Durrer D, Van Dam RT, Freud G, Janse MJ, Meijler FL, Arzbaecher RC (1970) Total excitation of the isolated human heart. *Circulation* 41(6):899–912
 33. Hyde ER, Behar JM, Claridge S, Jackson T, Lee AW, Remme EW, Sohal M, Plank G, Razavi R, Rinaldi CA, Niederer SA (2015) Beneficial effect on cardiac resynchronization from left ventricular endocardial pacing is mediated by early access to high conduction velocity tissue. *Circulation: Arrhythmia and Electrophysiology* 8(5):1164–1172
 34. Taccardi B, Punske BB, Macchi E, MacLeod RS, Ershler PR (2008) Epicardial and intramural excitation during ventricular pacing: effect of myocardial structure. *AJP - Heart Circ Physiol* 294(4):H1753–H1766
 35. Geneser SE, Kirby RM, MacLeod RS (2007) Application of stochastic finite element methods to study the sensitivity of ECG forward modeling to organ conductivity. *IEEE Trans Biomed Eng* 55(1):31–40
 36. Swenson D, Geneser S, Stinstra J, Kirby R, MacLeod R (2011) Cardiac position sensitivity study in the electrocardiographic forward problem using stochastic collocation and BEM. *J-ABE* 30:2900–2910
 37. Burk KM, Narayan A, Orr JA (2020) Efficient sampling for polynomial chaos-based uncertainty quantification and sensitivity analysis using weighted approximate Fekete points. *Int J Num Methods Biomed Eng* 36:e3395
 38. Rodero C, Strocchi M, Marciniak M, Longobardi S, Whitaker J, O'Neill MD, Gillette K, Augustin C, Plank G, Vigmond EJ et al (2021) Linking statistical shape models and simulated function in the healthy adult human heart. *PLoS Comput Biol* 17(4):e1008851
 39. Winkler B, Nagel C, Farchmin N, Heidenreich S, Loewe A, Dössel O, Bär M (2022) Global sensitivity analysis and uncertainty quantification for simulated atrial electrocardiograms. *Metrology* 3(1):1–28
 40. Lazarus A, Dalton D, Husmeier D, Gao H (2022) Sensitivity analysis and inverse uncertainty quantification for the left ventricular passive mechanics. *Biomech Model Mechanobiol* 21(3):953–982
 41. Karabelas E, Longobardi S, Fuchsberger J, Razeghi O, Rodero C, Strocchi M, Rajani R, Haase G, Plank G, Niederer S (2022) Global sensitivity analysis of four chamber heart hemodynamics using surrogate models. *IEEE Trans Biomed Eng* 69(10):3216–3223
 42. Strocchi M, Longobardi S, Augustin CM, Gsell MA, Petras A, Rinaldi CA, Vigmond EJ, Plank G, Oates CJ, Wilkinson RD et al (2023) Cell to whole organ global sensitivity analysis on a four-chamber heart electromechanics model using Gaussian processes emulators. *PLoS Comput Biol* 19(6):e1011257
 43. Gillette K, Winkler B, Kurath-Koller S, Scherr D, Vigmond EJ, Bär M, Plank G (2024) A computational study on the influence of antegrade accessory pathway location on the 12-lead electrocardiogram in Wolff-Parkinson-White syndrome. *Europace*, p euae223
 44. Sudret B (2008) Global sensitivity analysis using polynomial chaos expansions. *Reliability engineering & system safety* 93(7):964–979
 45. Narayan A, Liu Z, Bergquist JA, Charlebois C, Rampersad S, Rupp L, Brooks D, White D, Tate J, MacLeod RS (2023) UncertainSCI: Uncertainty quantification for computational models in biomedicine and bioengineering. *Comput Biol Med* 152:106407
 46. Gillette K, Gsell MA, Bouyssier J, Prassl AJ, Neic A, Vigmond EJ, Plank G (2021) Automated framework for the inclusion of a

- His-Purkinje system in cardiac digital twins of ventricular electrophysiology. *Ann Biomed Eng* 49(12):3143–3153
47. Tate J, Burton B, Khan A (2016) Seg3D basic functionality. http://www.sci.utah.edu/devbuilds/seg3d_docs/Seg3DBasicFunctionality.pdf Accessed 18 April 2017
 48. Zenger B, Good WW, Bergquist JA, Burton BM, Tate JD, Berkenbile L, Sharma V, MacLeod RS (Dec.2020) Novel experimental model for studying the spatiotemporal electrical signature of acute myocardial ischemia: A translational platform. *Physiol Meas* 41:15002
 49. CIBC (2016) Cleaver: A MultiMaterial Tetrahedral Meshing Library and Application. Scientific Computing and Imaging Institute (SCI), Download from: <http://www.sci.utah.edu/cibc/software.html>
 50. Bayer JD, Blake RC, Plank G, Trayanova NA (2012) A novel rule-based algorithm for assigning myocardial fiber orientation to computational heart models. *Ann Biomed Eng* 40:2243–2254
 51. Lombaert H, Peyrat J-M, Croisille P, Rapacchi S, Fanton L, Cheriet F, Clarysse P, Magnin I, Delingette H, Ayache N (2012) Human atlas of the cardiac fiber architecture: study on a healthy population. *EEE TMI* 31(7):1436–1447
 52. Stephenson RS, Atkinson A, Kottas P, Perde F, Jafarzadeh F, Bateman M, Iaizzo PA, Zhao J, Zhang H, Anderson RH et al (2017) High resolution 3-dimensional imaging of the human cardiac conduction system from microanatomy to mathematical modeling. *Sci Rep* 7(1):1–13
 53. Kléber AG, Rudy Y (2004) Basic Mechanisms of Cardiac Impulse Propagation and Associated Arrhythmias. *Physiol Rev* 84:431–488. Publisher: American Physiological Society
 54. Ideker RE, Kong W, Pogwizd S (2009) Purkinje fibers and arrhythmias. *Pacing and clinical electrophysiology PACE* 32:283–285
 55. Han B, Trew ML, Zgierski-Johnston CM (2021) Cardiac Conduction Velocity, Remodeling and Arrhythmogenesis. *Cells* 10:2923
 56. Tate J, Liu Z, Bergquist JA, Rampersad S, White D, Charlebois C, Rupp L, Brooks DH, MacLeod RS, Narayan A (2023) UncertainSCI: A Python Package for NoninvasiveParametric Uncertainty Quantification of Simulation Pipelines. *J Open Source Softw* 8:4249
 57. Xiu D, Karniadakis G (2002) Modeling uncertainty in steady state diffusion problems via generalized polynomial chaos. *Comput Methods Appl Mech Eng* 191:4927–4948
 58. Konukoglu E, Relan J, Cilingir U, Menze B, Chinchapatnam P, Jaidi A, Cochet H, Hocini M, Delingette H, Jaïs P et al (2011) Efficient probabilistic model personalization integrating uncertainty on data and parameters: Application to eikonal-diffusion models in cardiac electrophysiology. *Prog Biophys Mol Biol* 107(1):134–146
 59. Tanner L, Busatto A, Bergquist J, Good W, Zenger B, Plank G, Gillette K, MacLeod R (2025) The impact of hyperparameters in polynomial chaos expansion for uncertainty quantification in cardiac modeling. *j-CET*. Manuscript in Review
 60. Busatto A, Rupp LC, Gillette K, Plank G, Narayan A, MacLeod RS (2024) Application of order and sample selection in uncertainty quantification of cardiac models. In: 2024 Computing in Cardiology (CinC), pp 1–4. IEEE
 61. Vigmond E, Dos Santos RW, Prassl A, Deo M, Plank G (2008) Solvers for the cardiac bidomain equations. *Prog Biophys Mol Biol* 96(1–3):3–18
 62. He J, Pertsov AM, Cherry EM, Fenton FH, Roney CH, Niederer SA, Zang Z, Mangharam R (2023) Fiber Organization has Little Effect on Electrical Activation Patterns during Focal Arrhythmias in the Left Atrium. *IEEE Trans Biomed Eng* 70:1611–1621
 63. Tanner LCR, Busatto A, Bergquist JA, Good WW, Zenger B, Plank G, Narayan A, Gillette K, MacLeod RS (2025) Uncertainty quantification via polynomial chaos expansion of myocardial fibre orientation and cardiac activation patterns. *J Physiol* vol n/a, no n/a
 64. Norouzi S, Goudarzi T (2022) Effects of fiber orientation and the anisotropic behavior of the cardiac tissue on the simulated electrocardiogram. *Acta Mech* 233:3881–3892
 65. Zenger B, Good WW, Bergquist JA, Rupp LC, Perez MD, Stoddard GJ, Sharma V, Macleod RS (2021) Transient Recovery of Epicardial and Torso ST-Segment Ischemic Signals During Cardiac Stress Tests: A Possible Physiological Mechanism. *J Electrocardiol*, vol 69
 66. Panizo JG, Barra S, Mellor G, Heck P, Agarwal S (2018) Premature Ventricular Complex-induced Cardiomyopathy. *Arrhythmia & Electrophysiology Review* 7:128–134
 67. Alexander C, Bishop MJ, Gilchrist RJ, Burton FL, Smith GL, Myles RC (2023) Initiation of ventricular arrhythmia in the acquired long QT syndrome. *Cardiovasc Res* 119:465–476
 68. Calo' L, Tatangelo M, Panattoni G, Crescenzi C, Squeglia M, Fanisio F, Romeo F, Toto F, de Ruvo E, Rebecchi M (2024) Unlocking the enigma: decoding premature ventricular complexes for effective clinical assessment and risk management. *Eur Heart J Suppl* 26:i23–i28
 69. Burri H, Jastrzebski M, Cano O, Curila K, de Pooter J, Huang W, Israel C, Joza J, Romero J, Vernoooy K, Vijayaraman P, Whinnett Z, Zanon F (2023) EHRA clinical consensus statement on conduction system pacing implantation: endorsed by the Asia Pacific Heart Rhythm Society (APHRs), Canadian Heart Rhythm Society (CHRS), and Latin American Heart Rhythm Society (LAHRS). *Europace* 25:1208–1236

Publisher's Note Springer Nature remains neutral with regard to jurisdictional claims in published maps and institutional affiliations.

Springer Nature or its licensor (e.g. a society or other partner) holds exclusive rights to this article under a publishing agreement with the author(s) or other rightsholder(s); author self-archiving of the accepted manuscript version of this article is solely governed by the terms of such publishing agreement and applicable law.

Anna Busatto PhD, graduated in Biomedical Engineering at the University of Utah, specializing in computational cardiac modeling and uncertainty quantification for digital-twin applications.

Lindsay C. R. Tanner PhD, graduated in Biomedical Engineering from the University of Utah, specializing in computational cardiac modeling and uncertainty quantification.

Jake Bergquist PhD, is a research computer scientist and an adjunct assistant professor in the Department of Biomedical Engineering at the University of Utah.

Gernot Plank PhD, is a professor of Computational Cardiology at the Medical University of Graz with extensive experience in computational modeling and cardiac electrophysiology.

Karli Gillette PhD, is a tenure-track assistant professor in the Department of Biomedical Engineering at the University of Utah, specializing in patient-specific models of cardiac electrophysiology.

Akil Narayan PhD, is a professor in the Department of Mathematics at the University of Utah. His research focuses on uncertainty quantification (UQ), numerical analysis, and scientific computing.

Rob S. MacLeod PhD, is the director of the Scientific Computing and Imaging Institute. His research focuses on cardiac electrophysiology and the application of UQ to simulations of bioelectric fields.